



Cite this: *Nanoscale*, 2023, **15**, 4940

## Homogeneous in-plane WSe<sub>2</sub> P–N junctions for advanced optoelectronic devices†

Dewu Yue,<sup>a</sup> Xin Ju,<sup>\*b</sup> Tao Hu,<sup>a</sup> Ximing Rong,<sup>id</sup> c Xinke Liu,<sup>c</sup> Xiao Liu,<sup>c</sup> Hong Kuan Ng,<sup>b</sup> Dongzhi Chi,<sup>b</sup> Xinzhong Wang<sup>\*a</sup> and Jing Wu<sup>id</sup> <sup>\*b,d</sup>

Conventional doping schemes of silicon (Si) microelectronics are incompatible with atomically thick two-dimensional (2D) transition metal dichalcogenides (TMDCs), which makes it challenging to construct high-quality 2D homogeneous p–n junctions. Herein, we adopt a simple yet effective plasma-treated doping method to seamlessly construct a lateral 2D WSe<sub>2</sub> p–n homojunction. WSe<sub>2</sub> with ambipolar transport properties was exposed to O<sub>2</sub> plasma to form WO<sub>x</sub> on the surface in a self-limiting process that induces hole doping in the underlying WSe<sub>2</sub> via electron transfer. Different electrical behaviors were observed between the as-exfoliated (ambipolar) region and the O<sub>2</sub> plasma-treated (p-doped) region under electrostatic modulation of the back-gate bias (V<sub>BG</sub>), which produces a p–n in-plane homojunction. More importantly, a small contact resistance of 710 Ω μm with a p-doped region transistor mobility of ~157 cm<sup>2</sup> V<sup>-1</sup> s<sup>-1</sup> was achieved due to the transformation of Schottky contact into Ohmic contact after plasma treatment. This effectively avoids Fermi-level pinning and significantly improves the performance of photodetectors. The resultant WSe<sub>2</sub> p–n junction device thus exhibits a high photoresponsivity of ~7.1 × 10<sup>4</sup> mA W<sup>-1</sup> and a superior external quantum efficiency of ~228%. Also, the physical mechanism of charge transfer in the WSe<sub>2</sub> p–n homojunction was analyzed. Our proposed strategy offers a powerful route to realize low contact resistance and high photoresponsivity in 2D TMDC-based optoelectronic devices, paving the way for next-generation atomic-thickness optoelectronics.

Received 9th November 2022,  
 Accepted 25th January 2023

DOI: 10.1039/d2nr06263a

rscl.li/nanoscale

## 1. Introduction

Two-dimensional (2D) materials, such as transition metal dichalcogenides (TMDCs), hold promise as fundamental building blocks for next-generation flexible electronic and optoelectronic devices because of their tunable bandgap, high mobility, good chemical stability, and ability to form high-quality interfaces in van der Waals (vdW) heterostructures.<sup>1–5</sup> Among all TMDCs, WSe<sub>2</sub> is an intriguing 2D material that offers bipolar transport characteristics with thickness-dependent band gaps of 1.7 eV (direct, monolayer) and approxi-

mately 1.2 eV (indirect, multilayer), as well as theoretical electron and hole mobilities of about 250 and 270 cm<sup>2</sup> V<sup>-1</sup> s<sup>-1</sup>, respectively.<sup>6–8</sup> Owing to its unique physical properties, WSe<sub>2</sub> has opened the door to versatile electronic and optoelectronic devices with excellent optoelectronic performance. In recent years, new artificial structures based on van der Waals (vdW) vertical heterostructures or lateral p–n heterojunctions have attracted great interest in the application of WSe<sub>2</sub> optoelectronic devices.<sup>9–14</sup> For instance, Jo and co-workers demonstrated that the photoresponsivity of WSe<sub>2</sub>/h-BN-based p–n heterojunction photodetectors was remarkably improved by a triphenylphosphine n-doping method.<sup>15</sup> Guo and co-workers reported that a WSe<sub>2</sub>–ZnO p–n heterojunction photodetector fabricated by combining p-type WSe<sub>2</sub> and n-type ZnO exhibited an ultra-high photoresponsivity of 4.83 × 10<sup>3</sup> A W<sup>-1</sup> under 405 nm light illumination.<sup>16</sup> Liu *et al.* reported that a photodetector based on a WSe<sub>2</sub>–Bi<sub>2</sub>Te<sub>3</sub> p–n heterojunction can give rise to a fast response time of ~210 μs and a high photoresponsivity of ~20.5 A W<sup>-1</sup> under 633 nm illumination.<sup>17</sup> These results have demonstrated that the successful construction of heterojunctions can significantly improve the photo-response characteristics of TMDC-based devices, which, however, still suffer from unavoidable residues and complex flake alignment processes, *i.e.*, difficult to localize the target

<sup>a</sup>Information Technology Research Institute, Shenzhen Institute of Information Technology, Shenzhen, 518172, China. E-mail: wangxz@szitit.com.cn

<sup>b</sup>Institute of Materials Research and Engineering (IMRE), Agency for Science, Technology and Research (A\*STAR), 2 Fusionopolis Way, Innovis #08-03, Singapore 138634, Singapore. E-mail: ju\_xin@imre.a-star.edu.sg, wujing@imre.a-star.edu.sg

<sup>c</sup>College of Materials Science and Engineering, Shenzhen Key Laboratory of Special Functional Materials, Shenzhen Engineering Laboratory for Advanced Technology of Ceramics, Guangdong Research Center for Interfacial Engineering of Functional Materials, Shenzhen University, Shenzhen 518060, China

<sup>d</sup>Department of Materials Science and Engineering, National University of Singapore, 9 Engineering Drive 1, Singapore 117575, Singapore

† Electronic supplementary information (ESI) available. See DOI: <https://doi.org/10.1039/d2nr06263a>



material onto another flake accurately.<sup>18</sup> In addition, the presence of a vdW gap between junctions may inhibit carrier charge transfer, which is generally undesirable for the device performance. As an alternative strategy, homogeneous junctions offer intrinsic advantages over heterogeneous junctions by providing clean and self-aligned interfaces.

Since the Fermi level ( $E_F$ ) of WSe<sub>2</sub> resides in the middle of the band gap, its ambipolar nature allows for electron or hole dominant transport *via* selective doping, which can be used as an ideal candidate for the implementation of p–n photodiodes, photovoltaic cells, and complementary logic systems.<sup>19–23</sup> However, the *in situ* synthesis of high-quality homogeneous WSe<sub>2</sub> p–n junction-based photodetectors still faces many hurdles, such as the complex fabrication process, slow photoresponsivity, low photodetectivity, *etc.* On the other hand, the formation of a Schottky barrier (SB) at the WSe<sub>2</sub>–metal interface inevitably results in a high contact resistance ( $R_c$ ).<sup>24,25</sup> Furthermore, the physical metal deposition process may cause potential lattice disorders or even local destruction of the material, leading to Fermi-level pinning or poor band alignment, ultimately limiting the efficiency of photodiodes.<sup>26–28</sup> Consequently, carrier transport can only be carried out by tunneling through thin SBs, resulting in a low current density. To overcome the inherent performance limits of 2D TMDCs and to improve the contact problems on WSe<sub>2</sub> functional devices, various doping schemes, work function engineering techniques, electrical tuning techniques, *etc.* have been explored.<sup>29–35</sup> However, these methods are relatively complicated and require high temperature or vacuum process conditions, which greatly hinder their practical application in constructing high-performance WSe<sub>2</sub>-based photodetectors. Most recently, transition metal oxides (TMOs) used in organic electronics and 2D material-based electronic devices have been demonstrated as effective p-type contacts and dopants.<sup>36,37</sup> This doping scheme has been widely developed and applied in

complementary metal–oxide–semiconductor (CMOS) technology. Despite many encouraging outcomes so far, the fabrication of a 2D TMDC p–n homojunction with low  $R_c$  is still limited by technical challenges.

In this work, we demonstrate an efficient and reliable approach by performing O<sub>2</sub> plasma treatment to easily permit the amplification of hole transport, and thus achieve *in situ* p-type semiconductor characteristics in WSe<sub>2</sub>. The under-stoichiometric oxidation of WSe<sub>2</sub> into WO<sub>x</sub> highly induces hole doping in the neighboring (or underlying) WSe<sub>2</sub> *via* electron transfer from the underlying WSe<sub>2</sub> to the top oxidized WO<sub>x</sub> layer. Moreover, our results revealed that the transformation of the SB to Ohmic contact arising from plasma treatment greatly increases the hole mobility from  $\sim 22$  to  $\sim 157$  cm<sup>2</sup> V<sup>-1</sup> s<sup>-1</sup> in a p-type doped WSe<sub>2</sub> transistor. As a result, the as-fabricated in-plane p–n homojunction exhibits a superior external quantum efficiency of  $\sim 228\%$ , an excellent photoresponsivity of  $\sim 7.1 \times 10^4$  mA W<sup>-1</sup>, and a photodetectivity of  $\sim 3 \times 10^3$  Jones under 532 nm light illumination. The resultant device performance of our method proves it to be an ideal strategy for constructing high-performance p–n junction optoelectronic devices by using self-oxidizing 2D TMDCs, which may be applied to other TMDCs for future multifunctional electronic and optoelectronic applications.

## 2. Results and discussion

Fig. 1(a) shows the schematic illustration of a pristine and plasma-treated WSe<sub>2</sub>. The WSe<sub>2</sub> flake was treated with physical O<sub>2</sub> plasma bombardment where the Se atoms were replaced by O atoms, which then forms a WO<sub>x</sub> layer on the surface of the WSe<sub>2</sub> flake. The same sample was repeatedly subjected to plasma treatment, and the transfer characteristics of the as-fabricated WSe<sub>2</sub> FET at cumulative plasma durations of 5 to 120 s were measured (Fig. S1†). A change in the majority of carriers, from electrons to holes (n-dominant ambipolar to strong p-type), is observed with an on/off ratio reaching 10<sup>8</sup> after 120 s of O<sub>2</sub> plasma treatment as shown in Fig. S1.† As a result, the topmost layers of the WSe<sub>2</sub> flake were completely oxidized into WO<sub>x</sub>, consistent with previous reports where WO<sub>x</sub> is used as an effective doping layer.<sup>23</sup> In addition, the thickness of the WSe<sub>2</sub> flakes increased by  $\sim 1$  nm after O<sub>2</sub> plasma treatment (Fig. 1(b)), which is an indication of the formation of a thin layer of WO<sub>x</sub> atop the WSe<sub>2</sub> flake. The oxidation depth of the WSe<sub>2</sub> flake was subsequently assessed using the secondary-ion mass spectrometry (SIMS) technique. As shown in Fig. S2,† oxidation is found to be a self-limiting process. The depth of the oxide layer (WO<sub>x</sub>, including WO<sup>-</sup>, WO<sub>2</sub><sup>-</sup>, and WO<sub>3</sub><sup>-</sup>) is determined to be approximately 1.2 nm, which is restricted only in the very top layer, therefore offering an easy and efficient control of the oxide thickness. To further validate the formation of the WO<sub>x</sub> layer, the surface composition of the plasma-treated WSe<sub>2</sub> was further analyzed using X-ray photoelectron spectroscopy (XPS), as presented in Fig. 1(c). The XPS core spectrum of the pristine WSe<sub>2</sub> shows



Jing Wu

*Dr Jing Wu received his bachelor's degree in Physics from Zhejiang University in 2010 and his PhD in physics from the National University of Singapore (NUS) in 2015. He is currently the group leader of the Nano Electronic and Thermal Transport (NETT) group at the Institute of Materials Research and Engineering (IMRE) and an adjunct faculty member in the Department of Materials Science and Engineering, NUS. His*

*research interests focus on the exotic transport dynamics and scattering physics of 2D materials, such as charge transport, thermoelectric and optoelectronic transport, and exploring the technical aspects for high-performance electronics.*





**Fig. 1** (a) Schematic illustration of O<sub>2</sub> plasma treatment of bulk WSe<sub>2</sub>. (b) The AFM images of a WSe<sub>2</sub> flake before and after O<sub>2</sub> plasma treatment, and the right part shows the AFM height profile revealing the thickness of the ~13 nm WSe<sub>2</sub> flake. (c) The XPS spectral comparison shows the existence of one extra peak at a binding energy of 36.50 eV corresponding to WO<sub>x</sub> and a slight shift in the binding energies of W peaks after O<sub>2</sub> plasma treatment. (d) Transfer characteristics of a WSe<sub>2</sub> FET with V<sub>d</sub> = 1 V before and after O<sub>2</sub> plasma treatment. The inset shows the optical image of the as-fabricated WSe<sub>2</sub> FET. (e) The mobility obtained from WSe<sub>2</sub> FETs of different thicknesses.

two main peaks at 27.82 and 31.20 eV corresponding to W 4f<sub>7/2</sub> and W 4f<sub>5/2</sub>, respectively.<sup>38,39</sup> In comparison, the W 4f<sub>7/2</sub> (28.11 eV) and W 4f<sub>5/2</sub> (31.49 eV) peaks of the plasma-treated WSe<sub>2</sub> showed a slight shift to higher binding energies. Moreover, a clear additional peak can be observed at the binding energy of 36.50 eV corresponding to WO<sub>x</sub> (x ≤ 3),<sup>40</sup> which verifies the presence of WO<sub>x</sub> at the top of WSe<sub>2</sub> flakes. These results

demonstrate that oxygen radicals are efficiently doped into WSe<sub>2</sub> crystals during plasma exposure. Furthermore, the transport characteristics of the pristine and plasma-treated WSe<sub>2</sub>-based FETs were investigated under an applied gate voltage from -60 to 60 V. The optical microphotograph of the plasma treated WSe<sub>2</sub> based-FET is presented in the inset of Fig. 1(d). The pristine WSe<sub>2</sub>-based FET exhibits n-type dominated ambi-



polar characteristics, as shown in Fig. 1(d). However, after O<sub>2</sub> plasma treatment, the transfer curve shows a heavily p-doped characteristic (Fig. 1(d)). These results confirm the modulation of the as-fabricated WSe<sub>2</sub> channels with O<sub>2</sub> plasma, which act as p-type dopants when exposed to controlled plasma conditions.<sup>41</sup> The field-effect mobility ( $\mu_{FE}$ ) can be calculated from the following formula  $\mu_{FE} = g_m L_c h / C_{ox} W_{ch} V_{SD}$ ,<sup>42</sup> where  $L_{ch}$  and  $W_{ch}$  are the channel length and width, respectively,  $C_{ox} = 1.15 \times 10^{-8}$  F cm<sup>-2</sup> for 300 nm SiO<sub>2</sub>,  $g_m = \partial I_D / \partial V_{BG}$  is the transconductance, and  $V_{SD}$  is the source–drain voltage. The maximum  $\mu_{FE}$  of the as-fabricated WSe<sub>2</sub> FETs is found to be about 157 cm<sup>2</sup> V<sup>-1</sup> s<sup>-1</sup>, which is much higher than previously reported results (see Table 1). Fig. 1(e) shows the  $\mu_{FE}$  of the pristine and O<sub>2</sub>-treated WSe<sub>2</sub> devices fabricated with different thicknesses from 5 nm to 30 nm, where the FET mobility is significantly increased by up to a factor of 8 after O<sub>2</sub> plasma-induced p-type doping. We believe that the high mobility obtained may be attributed to the lowering of the contact resistance ( $R_c$ ) by plasma doping.

It is well-known that a high contact resistance  $R_c$  would significantly affect the electrical and optical performances of TMDC-based FETs.<sup>30</sup> Hence, we fabricated devices with the same channel width and different channel lengths ranging from 2 to 5  $\mu$ m to evaluate the contact  $R_c$  of the p-doped WSe<sub>2</sub> channels by the transmission line method (TLM). Fig. 2(a) shows the optical images of the WSe<sub>2</sub> devices with varied channel lengths for examining contact properties. The enlarged schematic in Fig. 2(a) illustrates the carrier pathways (yellow arrows) in the channel of the plasma-treated device, where the electron transfer from the underlying WSe<sub>2</sub> to the surface WO<sub>x</sub> contributes to the formation of electron transport paths (red arrows) from the channel to the doping layer, which is consistent with previous reports.<sup>23,43,44</sup> In particular, a thin WO<sub>x</sub> layer formed after the oxygen plasma treatment will attract electrons from the neighboring (or underlying) WSe<sub>2</sub>, thereby inducing the heavily p-doped WSe<sub>2</sub>, *i.e.*, the formation of a conducting channel of holes. The transfer characteristics of these devices are shown in Fig. S3.† Fig. 2(b) and (c) show the output characteristics obtained from the pristine and O<sub>2</sub> plasma-treated WSe<sub>2</sub>-based FETs, respectively. The non-linear

increase of hole current with increasing drain bias ( $V_D$ ) indicates a large SB between the metal and pristine WSe<sub>2</sub> layers (see Fig. 2(b)). In contrast, the excellent linear characteristics of the output curve of the O<sub>2</sub>-plasma treated WSe<sub>2</sub> layers in Fig. 2(c) suggest the conversion of Schottky contact into Ohmic-like behavior. This may be attributed to the shift of the Fermi level towards the valence band maximum (VBM) of WSe<sub>2</sub>: p-type dominant conversion. We believe that this phenomenon contributes to the transition from Schottky emission to direct tunneling for easier hole injection. For Schottky emission,<sup>45</sup>  $I = I_{SE} \exp(A\sqrt{V})$ , where  $I_{SE}$  and  $A$  (>0) are two parameters related to Schottky emission behavior. For F–N tunneling or FNT,<sup>46</sup>  $I = I_{FN} V^2 \exp(B/V)$ , where  $I_{FN}$  and  $B$  (<0) are two parameters related to F–N tunneling behavior. To better elucidate the transition from Schottky emission to direct tunneling, the  $I$ - $V$  curves are plotted in the forms of  $\ln I$ -vs.- $V^{1/2}$  and  $\ln(I/V^2)$ -vs.- $V^{-1}$ , respectively. Fig. S4† shows that before plasma treatment, the channel is dominated by Schottky emission, while after plasma treatment, the F–N tunneling becomes dominant. To further quantify the variation in  $R_c$  after plasma treatment, Fig. 2(d) shows the linear fitting of the total resistance ( $R_{total}$ ) as a function of channel length ( $L$ ).  $R_{total}$  could be described as  $R_{total} = LR_{ch}/W + 2R_c$ ,<sup>47</sup> where  $R_c$  is the contact resistance,  $W$  is the channel width,  $L$  is the channel length, and  $R_{ch}$  is the 2D channel resistance. The value of  $R_c$  can be directly extracted from the y-intercept of the linear fit to  $R_{total}$ . Fig. 2(e) shows  $R_c$  ranging from 0.71 to 6.73 k $\Omega$   $\mu$ m under different gate voltages ranging from -60 to 60 V. Considering the small thickness of the channel, uniform doping leads to a uniform current distribution in the vertical direction. A high gate bias leads to an increase in carrier density and the narrowing of the potential barrier along the metal and the material interface. The elevated hole concentration and narrowed potential barrier aid in the injection of carriers into the WSe<sub>2</sub> channel and thereby achieve a transition from Schottky emission to direct tunneling. As a result, a lower contact resistance is obtained.<sup>47</sup> In particular, the lowest  $R_c$  of  $\sim 710 \Omega \mu$ m measured at  $V_{BG} = -60$  V can be successfully achieved in the plasma-treated WSe<sub>2</sub> FETs, suggesting a reduction in  $R_c$  after the plasma treatment. It should be noted that such a small  $R_c$  highlights the importance of the self-terminating oxidation process, resulting in the thinnest oxide and therefore a transparent tunnel barrier for increased hole injection between the metal and WSe<sub>2</sub> as a key factor for the excellent device performance.

The p–n junction is crucial for the separation of photon-induced electron–hole (e–h) pairs towards achieving photo-detectors with high responsivity or solar cells with high quantum efficiency.<sup>48,49</sup> Through oxidation doping, the partial doping of a WSe<sub>2</sub> FET results in a lateral p–n homojunction. To determine their optoelectronic performance, WSe<sub>2</sub> lateral junctions were fabricated. More detailed information regarding the device preparation process can be found in the Experimental section. Fig. 3(a) shows the schematic diagram and the optical image (top-view) of the fabricated WSe<sub>2</sub> devices. These WSe<sub>2</sub> devices were then exposed to O<sub>2</sub> plasma

**Table 1** Comparison of the field-effect mobility with other WSe<sub>2</sub>-based electronic devices

Materials	Field-effect mobility (cm <sup>2</sup> V <sup>-1</sup> s <sup>-1</sup> )	Ref.
<b>WSe<sub>2</sub> pn-junction</b>	<b>157</b>	<b>This work</b>
WSe <sub>2</sub> /MoS <sub>2</sub> heterojunction	8.42	6
WSe <sub>2</sub> (1-x)Te <sub>2x</sub>	46	7
WSe <sub>2</sub> /ReS <sub>2</sub> pn-junction	16.5	10
WSe <sub>2</sub> pn-junction	36.28	11
Monolayer WSe <sub>2</sub>	132	13
WSe <sub>2</sub> /h-BN heterojunction	25.6	15
WO <sub>x</sub> /WSe <sub>2</sub> heterojunction	40	23
WSe <sub>2</sub> flake	2.2	24
WSe <sub>2</sub> /Graphene heterojunction	84	25
Monolayer WSe <sub>2</sub>	82	28
WSe <sub>2</sub> flake	150	35



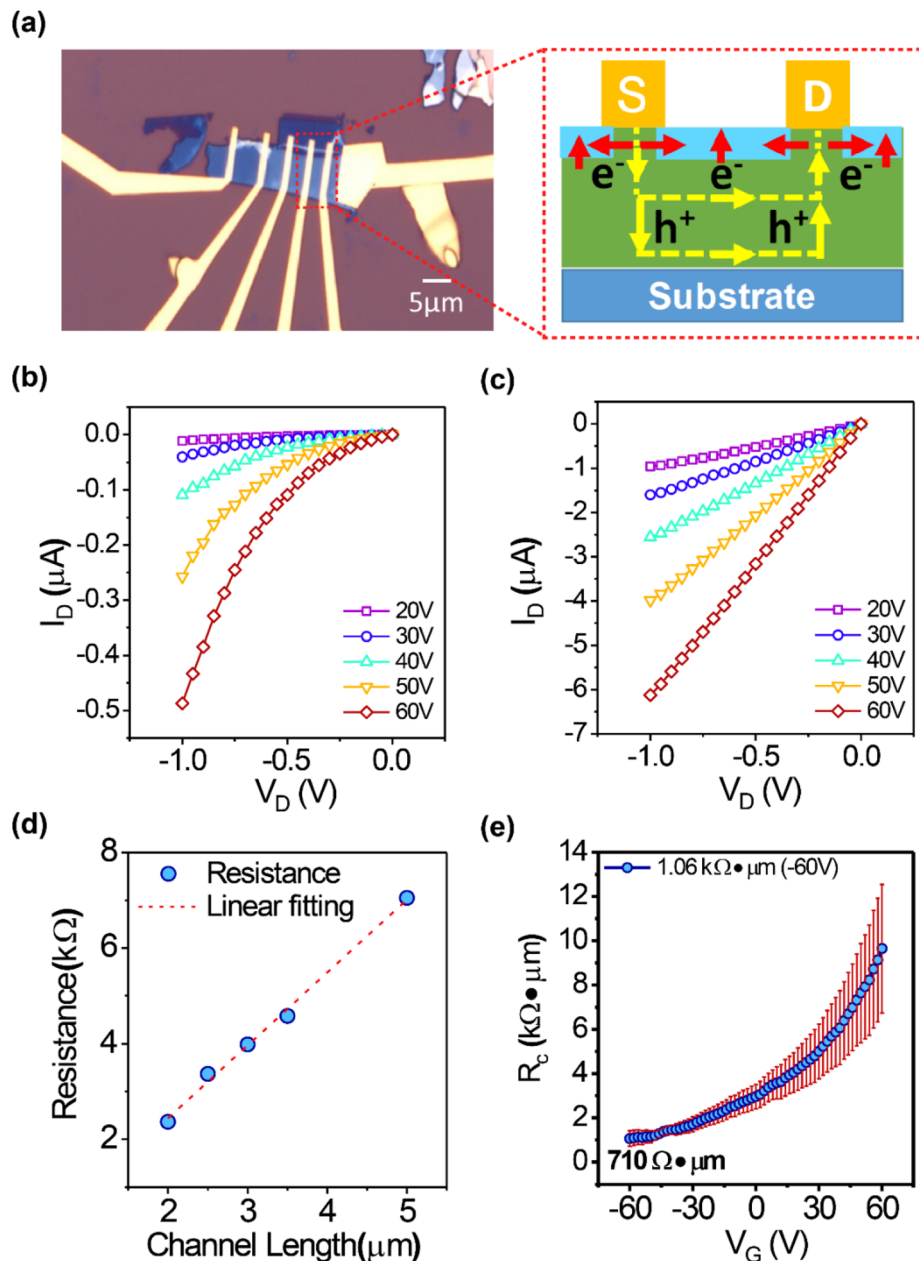


**Fig. 2** Contact properties of the WSe<sub>2</sub> FETs obtained by TLM measurement. (a) Optical micrograph of the TLM devices. The enlarged section on the right side shows the hole transport path occurring in the whole channel, which can lead to low contact resistance and thus higher mobility. (b) Schottky contact can be clarified from the output characteristics of the pristine WSe<sub>2</sub> FETs. (c) By applying O<sub>2</sub> plasma treatment, Ohmic contact was achieved in WSe<sub>2</sub> FETs. (d)  $R_{\text{total}}$  as a function of channel length to extract  $R_c$  using a TLM linear fitting curve. (e)  $R_c$  versus bottom gate voltage in which the lowest  $R_c$  obtained was  $\sim 710 \Omega \cdot \mu\text{m}$  at a  $V_{\text{BG}}$  of  $-60 \text{ V}$ .

under different operating conditions (see the Experimental section). Note that a PMMA layer is employed as a mask to protect areas with electrodes 1 to 2, leaving areas with electrodes marked with 3 to 4 exposed for O<sub>2</sub> plasma treatment. The O<sub>2</sub> molecule was then chemisorbed onto the top surface of the exposed WSe<sub>2</sub>, in which the top layer of the Se atom was substituted by an oxygen atom. Finally, the WO<sub>x</sub> layer was formed on top of the WSe<sub>2</sub> layer. As a result of p-doping due to O<sub>2</sub> plasma (formation of a WO<sub>x</sub> layer on the top of WSe<sub>2</sub>), a p-type

(n-type) dominant conduction is observed in the O<sub>2</sub> plasma-treated (plasma-protected) region. The typical transfer curves of the pristine WSe<sub>2</sub> channel (through electrodes 1 to 2) were measured to maintain n-type behaviour (Fig. 3(b)). The electrical performance of the as-prepared plasma-treated channel was then measured through electrodes 3 to 4 (Fig. 3(c) and Fig. S5†), yielding p-type characteristics. With the capability of achieving both unipolar p-type (plasma-treated) and n-type (pristine) conduction behaviours, a lateral p–n homojunction





**Fig. 3** (a) 3D schematic structure and optical photograph (right side) of an O<sub>2</sub> plasma-treated WSe<sub>2</sub> FET device showing channels 1–2, 2–3, and 3–4 as n-WSe<sub>2</sub>, pn-WSe<sub>2</sub>, and p-WSe<sub>2</sub>, respectively. (b) and (c) The transfer curves of n- and p-WSe<sub>2</sub> channels measured at V<sub>d</sub> = 1 V after O<sub>2</sub> plasma treatment, which are represented in both linear and logarithmic scales. (d) The output curve of an O<sub>2</sub> plasma-treated WSe<sub>2</sub> p–n junction device obtained at V<sub>g</sub> = –40 V is represented on a linear scale. (e) The output curve is represented on a logarithmic scale to calculate the p–n junction ideality factor as 1.4.

can then be fabricated using a single WSe<sub>2</sub> flake. Fig. 3(d) and (e) show the corresponding  $I_d - V_d$  output curves of the partially doped WSe<sub>2</sub> device (channel: electrodes 2–3) with V<sub>g</sub> = –40 V in the linear (left) and log (right) scales, in which little to no current flow is observed under reverse source–drain bias (V<sub>d</sub> < 0 V). However, a much higher current flow can be observed when a forward bias is applied (V<sub>d</sub> > 0 V), indicating the forward rectifying diode behavior. Furthermore, an ideality factor ( $n$ )<sup>50,51</sup> of 1.4 was calculated from the dark current (Fig. 3(e)), indicating the formation of a near-ideal p–n junction.<sup>52,53</sup> It is known that  $n = 1$  indicates an ideal p–n junction

diode,  $n$  ranging between 1 and 2 implies the existence of a tunneling current, and  $n = 2$  indicates the existence of defects or interface traps that drives the recombination process.<sup>54</sup> Thus, our good ideality factor of ~1.4 can be ascribed to the low charge trap density at the homojunction interface.<sup>55</sup> The above results prove the successful preparation of a p–n junction between electrodes 2 and 3. However, it should be noted that the p–n WSe<sub>2</sub> device is formed with a Schottky junction in the n-type part of WSe<sub>2</sub> (contact 2), p–n junctions in the channel (electrodes 2–3), and Ohmic-like contact in the p-type part of WSe<sub>2</sub> (contact 3).



Next, we explored the optoelectronic properties of p–n WSe<sub>2</sub> homojunction photodetectors. The transfer curves of the as-fabricated photodetector were measured in the dark and 532 nm illumination. By comparison, a photocurrent response characteristic under light irradiation is observed in Fig. 4(a), which may be mainly attributed to the strong light absorption in the WSe<sub>2</sub> p–n junction. This then generates a larger density of photoinduced e–h pairs which leads to a reduction of the Schottky barrier, thereby allowing the photogenerated carriers to transmit more effectively along the metal/WSe<sub>2</sub> interface under an externally applied bias. To further investigate the performance of WSe<sub>2</sub> p–n junction photodetectors and to study their dynamic optical response, time (*T*)- and gate voltage (*V<sub>G</sub>*)-dependent photocurrent measurements under a fixed source–drain bias of 1 V were performed as shown in Fig. 4(b). Here, the time (*T*)- and source–drain voltage (*V<sub>D</sub>*)-dependent photocurrent of the WSe<sub>2</sub> p–n junction photodetectors was also measured at the fixed gate bias of 40 V (Fig. 4(c)). As *V<sub>G</sub>* swept from +40 to –40 V, the photocurrent enhancement was observed under various *V<sub>D</sub>* and *V<sub>G</sub>* conditions. In particular, the maximum photocurrent is obtained under a gate bias voltage of 40 V. Meanwhile, prominent variations in the gate-dependent photocurrent can be obtained at both *V<sub>G</sub>* < 0 V and *V<sub>G</sub>* > 0 V sides. These results suggest that the photocurrent response can be effectively modulated by the gate electric field. In addition, the photocurrent is observed to slightly decrease with time under continuous light irradiation, indicating possible charge trapping effects. Higher gate voltage (40 V) leads to an increase in carrier concentration while the potential barrier at the contact interface becomes narrower. Thus, the charge trap states are relatively more easily filled with carriers, leading to a slight reduction in photocurrent. In contrast, at a gate voltage of 0 V, when the Fermi level is in equilibrium, the carrier density is relatively low. As such, carriers are difficult to be captured by trap states, so minimal photocurrent changes are observed in time-dependent photocurrent measurements (Fig. S6†). The photocurrent characteristics of the junction can be further understood through the energy band diagrams, as shown in Fig. 4(d)–(f). Fig. 4(d) shows the band diagram of the WSe<sub>2</sub> p–n junction in the equilibrium state. The Fermi level of the p-type area is near to the valence band, whereas the Fermi level of the n-type part is near to the conduction band. Under reverse bias, the energy barrier at the junction becomes higher as the width of the depletion region increases. Consequently, electrons cannot transmit effectively, and the p–n junction is in the OFF state. Under forward bias, the energy barrier becomes lower, thus allowing electrons to easily pass through the junction, and the p–n junction is in the ON state. This typical p–n junction behavior is consistent with the output curve as shown in Fig. 3(d). Furthermore, the mechanism of photocurrent generated in the dark (Fig. 4(e)) and light (Fig. 4(f)) states was also proposed. When the negative gate voltage is applied in the dark state (Fig. 4(e)), the Fermi level drops below the valence band of the p-type branch, which enables holes to flow easily from the junction into the metal. As a result,

there is no current in the p–n junction. When a positive gate voltage is applied, the Fermi level moves into the conduction band in the n-type branch, which allows electrons to easily transfer from the junction into the metal. Therefore, the designed lateral p–n junction shows no current when electrons are dominant carriers. Under light irradiation, the generation of e–h pairs takes place near the depletion region, and the photoexcited carriers are swept from the junction in opposite directions by an externally applied bias, resulting in a net increase in photocurrent, as shown in Fig. 4(f). As a result, internal hole and electron transport combined with the resulting overdose e–h pairs from light absorption increases the current, which is much higher than the dark state (as shown in Fig. 4(e)) even at low gate voltages. In both positive and negative gate biases, the photocurrent is high as the substantial photogenerated e–h pairs can be readily separated and driven toward the cathode and anode contacts in the *in situ* WSe<sub>2</sub> lateral p–n junction.

Next, we further investigated the photoresponse of the designed WSe<sub>2</sub> p–n junction by measuring the *I<sub>D</sub>*–*V<sub>D</sub>* characteristics at the gate bias of –40 V and 40 V, respectively. Under different powers of light illumination (6, 16, 31, and 42 mW), the WSe<sub>2</sub> p–n junction exhibited ideal diode characteristics as shown in Fig. 4(g) and (h). The photoresponse figures of merit such as photoresponsivity (*R*), external quantum efficiency (EQE), and detectivity (*D*<sup>\*</sup>) are sequentially evaluated. The spectral responses of WSe<sub>2</sub> photodetectors were expressed through *R*, which is defined as the ratio of the photocurrent and the incident laser power, *i.e.*,  $R = I_{\text{ph}}/P_{\text{Laser}}$ , where *I<sub>ph</sub>* is the photocurrent =  $|I_{\text{light}} - I_{\text{dark}}|$ , and *P<sub>Laser</sub>* is the incident laser power per unit area. Here,  $I_{\text{ph}} = |I_{\text{light}} - I_{\text{dark}}| = 6 \times 10^{-6}$  A,  $P = L \cdot W / (\pi \cdot r^2) \cdot P_m = 3.5 \times 2.5 / (3.14 \times 30^2) \times 2.7 \times 10^{-5} = 8.4 \times 10^{-8}$  W, in which *L* and *W* are the channel length and channel width, *r* is the radius, and *P<sub>m</sub>* is the power measured by a power meter. Fig. 4(i) shows the photoresponsivities of the WSe<sub>2</sub> photodetector as a function of incident laser power. Another crucial figure of merit for the photodetector is the EQE, which is given by  $\text{EQE} (\%) = 100 \cdot hcR / e\lambda$ , where *h* is Planck's constant ( $6.63 \times 10^{-34}$  J s), *c* is the speed of light ( $3 \times 10^8$  m s<sup>-1</sup>), *e* is the unit charge, and *λ* is the wavelength of incident light (*λ* = 532 nm). The EQE of a photodetector represents the ratio of the total number of charge carriers generated to the number of incident photons. Through the above equations, the *R* and EQE of our p–n junction are calculated to be  $\sim 7.1 \times 10^4$  mA W<sup>-1</sup> and  $\sim 228\%$ , respectively, outperforming other reported results as summarized in Table 2.<sup>10,12,14–17,19,56–59</sup> The high values of *R* and EQE also demonstrate that the plasma-treated WSe<sub>2</sub> p–n junction exhibits a good photoresponsivity. In addition, *D*<sup>\*</sup> is another figure of merit for photodetector devices to evaluate the detector sensitivity, which is generally calculated using the following equation of  $D^* (\text{Jones}) = (R \cdot A^{1/2}) / (I_{\text{dark}} \cdot 2e)^{1/2}$ . The *D*<sup>\*</sup> value obtained for our designed WSe<sub>2</sub> p–n junction photodetector was about  $3 \times 10^3$  Jones. These results prove the effectiveness of O<sub>2</sub> plasma treatment for achieving high-performance WSe<sub>2</sub>-based optoelectronic devices.





**Fig. 4** (a) Typical photoresponse of the WSe<sub>2</sub> p-n homojunction FET devices under 532 nm illumination at different gate biases demonstrating clear photovoltaic behavior. (b) and (c) Time-dependent photocurrent measurements of pn-WSe<sub>2</sub> achieved under 532 nm laser irradiation at the applied  $V_d = 1$  V with various  $V_g$  values and fixed  $V_g = 40$  V with various  $V_d$  values. (d–f) The corresponding energy band diagrams show the carrier transport paths in the WSe<sub>2</sub> p-n homojunction device with and without light irradiation at the applied gate bias. (g) and (h) The photocurrents of the as-fabricated WSe<sub>2</sub> p-n homojunction under different powers of light illumination (5.35, 16, 31 and 42 mW) at gate biases of  $-40$  V and  $40$  V, respectively. (i) The photoresponsivity ( $R$ ) of the WSe<sub>2</sub> p-n junction obtained under gate biases of  $-40$  V and  $40$  V as a function of light power. The responsivity was linear with the incident optical power.





Table 2 Comparison of  $R$  with other  $\text{WSe}_2$ -based devices

Materials	Light irradiation conditions (nm)	$R$ ( $\text{mA W}^{-1}$ )	Response time (ms)	Ref.
<b><math>\text{WSe}_2</math> p-n junction</b>	532	$7.1 \times 10^4$	42	<b>This work</b>
$\text{WSe}_2/\text{ReS}_2$ p-n junction	532	$3 \times 10^3$	0.004	10
$\text{WSe}_2$ p-n junction	520	80	0.106	12
$\text{WSe}_2/\text{MoSe}_2$ heterojunction	1550	127		14
$\text{WSe}_2/\text{h-BN}$ junction	520	$1.27 \times 10^9$	38.2–97	15
$\text{WSe}_2/\text{ZnO}$ junction	405	$4.83 \times 10^6$	0.01	16
$\text{WSe}_2/\text{Bi}_2\text{Te}_3$ p-n junction	633	$2.05 \times 10^4$	0.21	17
p-Doped $\text{WSe}_2$	735	600	0.008	19
Multi-layer $\text{WSe}_2$	532	100	0.01	56
$\text{WSe}_2/\text{BP}/\text{MoS}_2$ heterojunction	532	$6.32 \times 10^3$		57
Multi-layer $\text{WSe}_2/\text{pentacene}$	638	$1.93 \times 10^4$		58
$\text{WSe}_2/\text{MoS}_2$ heterojunction	532	3.4		59

### 3. Conclusion

In summary, lateral p–n homojunctions were successfully fabricated from bulk  $\text{WSe}_2$  via oxygen plasma doping and demonstrated in gate-modulated photodetector applications. After the plasma treatment, the lowest  $R_c$  of  $\sim 710 \Omega \mu\text{m}$  of the  $\text{WSe}_2$  p–n junction can be achieved, which is attributed to the highly p-doped  $\text{WSe}_2$  that converts the Schottky barrier to Ohmic contact between the metal and  $\text{WSe}_2$  interface. Thanks to the low  $R_c$  and excellent mobility of  $\sim 157 \text{ cm}^2 \text{ V}^{-1} \text{ s}^{-1}$ , our plasma-treated  $\text{WSe}_2$  p–n junction exhibited an exceptional photoresponsivity of  $\sim 7.1 \times 10^4 \text{ mA W}^{-1}$ , a superior external quantum efficiency of  $\sim 228\%$ , and a detectivity of  $\sim 3 \times 10^3$  Jones under 532 nm light illumination wavelength. Our work provides an industry-compatible plasma doping technique to fabricate homogeneous in-plane p–n junctions for advanced 2-D optoelectronic device applications. Going forward, homogeneous complementary 2-D inverters can be fabricated by integrating the plasma-treated and as-exfoliated regions of a single  $\text{WSe}_2$  layer to create basic building blocks for logic circuits. Our results contribute toward the realization of the local plasma treatment of  $\text{WSe}_2$  flakes to tune the electrical properties of  $\text{WSe}_2$  and the feasibility of fabricating  $\text{WSe}_2$ -based optoelectronic logic applications.

### 4. Experimental section

#### Fabrication of pristine $\text{WSe}_2$ -based FETs and p-type $\text{WSe}_2$ -based FETs

The synthesis process of the pristine  $\text{WSe}_2$ -based device is given as follows: at first, the  $\text{WSe}_2$  film was exfoliated from the crystalline bulk material (HQ Graphene, the Netherlands) onto a 300 nm-thick  $\text{SiO}_2/\text{Si}$  substrate. Next, electrodes were patterned using electron beam lithography (EBL), and then deposited with Cr/Au (5 nm/70 nm) using an electron beam/thermal evaporator. To obtain p-type  $\text{WSe}_2$ -based FETs, the as-fabricated pristine  $\text{WSe}_2$ -based FETs were treated with  $\text{O}_2$  plasma (20 W, 120 s). Our used XPS model is Thermo Fisher (Microlab350) with magnesium light.

#### Fabrication of the $\text{WSe}_2$ p–n junction

The fabrication process of the  $\text{WSe}_2$  p–n junction is as follows: first, the pristine  $\text{WSe}_2$  device was spin-coated with PMMA (Microchem, A4 495) at a speed of 3000 rpm (60 s). The device was then annealed at 150 °C for 2 min on a hot plate. Afterward, another layer PMMA (Microchem, A6 950) was spin-coated on the top of PMMA A4 with the same process. Furthermore, to obtain the p–n junction structure, we used EBL along with a developer (mixed DI water and IPA solution at a ratio of 1 : 3) to open a channel near the electrode, followed by rinsing with IPA and drying under the  $\text{N}_2$  gas blowing. Finally,  $\text{O}_2$  plasma treatment is employed to treat the as-fabricated device to obtain the  $\text{WSe}_2$  p–n junction structure. The electrical transfer performances of the devices were tested in a vacuum probe station (Keithley 4200) at 0.1 Pa. The photocurrent response performance was measured using a light source of 532 nm.

#### Photocurrent measurement

Solid-state laser diodes were used as illumination sources. The incident power of the lasers ( $P_m$ ) was measured with an optical power meter (Newport model 1918-C) and a thermopile sensor (919P-003-10). We measured the photoresponse characteristics with a monochromator light source. The device was placed on the sample holder, and a continuous wave laser beam generated from the solid-state laser diode and controller (Thorlabs LPSC-520-FC and CLD1010LP for 520 nm (visible) and Thorlabs LPSC-852-FC and CLD1010LP for 852 nm (near IR)) was focused onto the device through a 40× objective lens (Olympus LUCPlanFLN, 40×, NA = 0.6).

### Conflicts of interest

The authors declare no conflict of interest.

### Acknowledgements

This work was supported by the National Natural Science Foundation of China (Grant No.12104319), the Shenzhen Science and technology planning project (JSGG20201102152403008), the



Double High-levels Plan (11400-2022-010201-02332) and the Science and Technology Project of Shenzhen City (JSGG20210802154213040). J. W. acknowledges the Advanced Manufacturing and Engineering Young Individual Research Grant (AME YIRG Grant No.: A2084c170) and the SERC Central Research Fund (CRF); J. W. and D. C. acknowledge the National Research Foundation Competitive Research Programme (NRFCRP24-2020-0002).

## References

- H. Xu, X. Han, X. Dai, W. Liu, J. Wu, J. Zhu, D. Kim, G. Zou, K. A. Sablon, A. Sergeev, Z. Guo and H. Liu, *Adv. Mater.*, 2018, **30**, 1706561.
- P. Gant, P. Huang, D. Pérez de Lara, D. Guo, R. Frisenda and A. Castellanos-Gomez, *Mater. Today*, 2019, **27**, 8–13.
- N. Flory, P. Ma, Y. Salamin, A. Emboras, T. Taniguchi, K. Watanabe, J. Leuthold and L. Novotny, *Nat. Nanotechnol.*, 2020, **15**, 118–124.
- H. K. Ng, D. Xiang, A. Suwardi, G. Hu, K. Yang, Y. Zhao, T. Liu, Z. Cao, H. Liu, S. Li, J. Cao, Q. Zhu, Z. Dong, C. K. I. Tan, D. Chi, C.-W. Qiu, K. Hippalgaonkar, G. Eda, M. Yang and J. Wu, *Nat. Electron.*, 2022, **5**, 489–496.
- T. Liu, D. Xiang, H. K. Ng, Z. Han, K. Hippalgaonkar, A. Suwardi, J. Martin, S. Garaj and J. Wu, *Adv. Sci.*, 2022, **9**(20), 2200816.
- G. H. Shin, C. Park, K. J. Lee, H. J. Jin and S. Y. Choi, *Nano Lett.*, 2020, **20**(8), 5741–5748.
- P. Yu, J. Lin, L. Sun, Q. L. Le, X. Yu, G. Gao, C. H. Hsu, D. Wu, T. R. Chang, Q. Zeng, F. Liu, Q. J. Wang, H. T. Jeng, H. Lin, A. Trampert, Z. Shen, K. Suenaga and Z. Liu, *Adv. Mater.*, 2017, **29**(4), 1603991.
- S. Ahmed, X. Ding, P. P. Murmu, N. Bao, R. Liu, J. Kennedy, L. Wang, J. Ding, T. Wu, A. Vinu and J. Yi, *Small*, 2020, **16**, 1903173.
- S. Jia, Z. Jin, J. Zhang, J. Yuan, W. Chen, W. Feng, P. Hu, P. M. Ajayan and J. Lou, *Small*, 2020, **16**, 2002263.
- A. Varghese, D. Saha, K. Thakar, V. Jindal, S. Ghosh, N. V. Medhekar, S. Ghosh and S. Lodha, *Nano Lett.*, 2020, **20**(3), 1707–1717.
- J. Sun, Y. Wang, S. Guo, B. Wan, L. Dong, Y. Gu, C. Song, C. Pan, Q. Zhang, L. Gu, F. Pan and J. Zhang, *Adv. Mater.*, 2020, **32**, 1906499.
- Y. Tang, Z. Wang, P. Wang, F. Wu, Y. Wang, Y. Chen, H. Wang, M. Peng, C. Shan, Z. Zhu, S. Qin and W. Hu, *Small*, 2019, **15**, 1805545.
- A. S. Bandyopadhyay, N. Adhikari and A. B. Kaul, *Chem. Mater.*, 2019, **31**(23), 9861–9874.
- H. Xue, Y. Wang, Y. Dai, W. Kim, H. Jussila, M. Qi, J. Susoma, Z. Ren, Q. Dai, J. Zhao, K. Halonen, H. Lipsanen, X. Wang, X. Gan and Z. Sun, *Adv. Funct. Mater.*, 2018, **28**, 1804388.
- S. H. Jo, D. H. Kang, J. Shim, J. Jeon, M. H. Jeon, G. Yoo, J. Kim, J. Lee, G. Y. Yeom, S. Lee, H. Y. Yu, C. Choi and J. H. Park, *Adv. Mater.*, 2016, **28**(24), 4824–4831.
- N. Guo, L. Xiao, F. Gong, M. Luo, F. Wang, Y. Jia, H. Chang, J. Liu, Q. Li, Y. Wu, Y. Wang, C. Shan, Y. Xu, P. Zhou and W. Hu, *Adv. Sci.*, 2020, **7**, 1901637.
- H. Liu, X. Zhu, X. Sun, C. Zhu, W. Huang, X. Zhang, B. Zheng, Z. Zou, Z. Luo, X. Wang, D. Li and A. Pan, *ACS Nano*, 2019, **13**(11), 13573–13580.
- R. Cheng, D. Li, H. Zhou, C. Wang, A. Yin, S. Jiang, Y. Liu, Y. Chen, Y. Huang and X. Duan, *Nano Lett.*, 2014, **14**(10), 5590–5597.
- T. Wang, K. Andrews, A. Bowman, T. Hong, M. Koehler, J. Yan, D. Mandrus, Z. Zhou and Y. Q. Xu, *Nano Lett.*, 2018, **18**(5), 2766–2771.
- D. Li, M. Chen, Z. Sun, P. Yu, Z. Liu, P. M. Ajayan and Z. Zhang, *Nat. Nanotechnol.*, 2017, **12**, 901–906.
- Y. Ren, X. Yang, L. Zhou, J. Y. Mao, S. T. Han and Y. Zhou, *Adv. Funct. Mater.*, 2019, **29**, 1902105.
- M. V. Gustafsson, M. Yankowitz, C. Forsythe, D. Rhodes, K. Watanabe, T. Taniguchi, J. Hone, X. Zhu and C. R. Dean, *Nat. Mater.*, 2018, **17**, 411–415.
- X. Liu, D. Qu, Y. Yuan, J. Sun and W. J. Yoo, *ACS Appl. Mater. Interfaces*, 2020, **12**(23), 26586–26592.
- S. J. Yang, K. T. Park, J. Im, S. Hong, Y. Lee, B. W. Min, K. Kim and S. Im, *Nat. Commun.*, 2020, **11**, 1574.
- H. L. Tang, M. H. Chiu, C. C. Tseng, S. H. Yang, K. J. Hou, S. Y. Wei, J. K. Huang, Y. F. Lin, C. H. Lien and L. J. Li, *ACS Nano*, 2017, **11**(12), 12817–12823.
- S. Fan, S. J. Yun, W. J. Yu and Y. H. Lee, *Adv. Sci.*, 2020, **7**, 1902751.
- S. W. LaGasse, P. Dhakras, K. Watanabe, T. Taniguchi and J. U. Lee, *Adv. Mater.*, 2019, **31**, 1901392.
- G. Dastgeer, M. F. Khan, G. Nazir, A. M. Afzal, S. Aftab, B. A. Naqvi, J. Cha, K. A. Min, Y. Jamil, J. Jung, S. Hong and J. Eom, *ACS Appl. Mater. Interfaces*, 2018, **10**(15), 13150–13157.
- H. G. Ji, P. Solis-Fernandez, D. Yoshimura, M. Maruyama, T. Endo, Y. Miyata, S. Okada and H. Ago, *Adv. Mater.*, 2019, **31**, 1903613.
- M. Si, C. Jiang, W. Chung, Y. Du, M. A. Alam and P. D. Ye, *Nano Lett.*, 2018, **18**(6), 3682–3687.
- G. Dastgeer, M. F. Khan, J. Cha, A. M. Afzal, K. H. Min, B. M. Ko, H. Liu, S. Hong and J. Eom, *ACS Appl. Mater. Interfaces*, 2019, **11**(11), 10959–10966.
- R. Zhou, V. Ostwal and J. Appenzeller, *Nano Lett.*, 2017, **17**(8), 4787–4792.
- H. Liu, D. Fu, X. Li, J. Han, X. Chen, X. Wu, B. Sun, W. Tang, C. Ke, Y. Wu, Z. Wu and J. Kang, *ACS Nano*, 2021, **15**(5), 8244–8251.
- A. M. Dibos, Y. Zhou, L. A. Jauregui, G. Scuri, D. S. Wild, A. A. High, T. Taniguchi, K. Watanabe, M. D. Lukin, P. Kim and H. Park, *Nano Lett.*, 2019, **19**(6), 3543–3547.
- E. V. Calman, L. H. Fowler-Gerace, D. J. Choksy, L. V. Butov, D. E. Nikonov, I. A. Young, S. Hu, A. Mishchenko and A. K. Geim, *Nano Lett.*, 2020, **20**(3), 1869–1875.
- Y. Huang, K. Yu, H. Li, K. Xu, Z. Liang, D. Walker, P. Ferreira, P. Fischer and D. E. Fan, *Adv. Mater.*, 2020, **32**, 2003439.



- 37 Z. Zheng, J. Chen, Y. Wang, X. Wang, X. Chen, P. Liu, J. Xu, W. Xie, H. Chen, S. Deng and N. Xu, *Adv. Mater.*, 2018, **30**, 1705318.
- 38 R. Zhang, D. Drysdale, V. Koutsos and R. Cheung, *Adv. Funct. Mater.*, 2017, **27**, 1702455.
- 39 X. Yu, N. Guijarro, M. Johnson and K. Sivula, *Nano Lett.*, 2018, **18**(1), 215–222.
- 40 H. Medina, J. G. Li, T. Y. Su, Y. W. Lan, S. H. Lee, C. W. Chen, Y. Z. Chen, A. Manikandan, S. H. Tsai, A. Navabi, X. Zhu, Y. C. Shih, W. S. Lin, J. H. Yang, S. R. Thomas, B. W. Wu, C. H. Shen, J. M. Shieh, H. N. Lin, A. Javey, K. L. Wang and Y. L. Chueh, *Chem. Mater.*, 2017, **29**, 1587.
- 41 B. Liu, Y. Ma, A. Zhang, L. Chen, A. N. Abbas, Y. Liu, C. Shen, H. Wan and C. Zhou, *ACS Nano*, 2016, **10**(5), 5153–5160.
- 42 C. Liu, G. Li, R. Di Pietro, J. Huang, Y.-Y. Noh, X. Liu and T. Minari, *Phys. Rev. Appl.*, 2017, **8**, 034020.
- 43 Z. Li, S. Yang, R. Dhall, E. Kosmowska, H. Shi, I. Chatzakis and S. B. Cronin, *ACS Nano*, 2016, **10**(7), 6836–6842.
- 44 T. D. Ngo, M. S. Choi, M. Lee, F. Ali, Y. Hassan, N. Ali, S. Liu, C. Lee, J. Hone and W. J. Yoo, *Adv. Sci.*, 2022, **9**, 2202465.
- 45 Y. Tian, C. Guo, S. Guo, T. Yu and Q. Liu, *Nano Res.*, 2014, **7**, 953–962.
- 46 Y. Tian, L. Jiang, X. Zhang, G. Zhang and Q. Zhu, *AIP Adv.*, 2018, **8**, 035105.
- 47 F. Xia, V. Perebeinos, Y. M. Lin, Y. Wu and P. Avouris, *Nat. Nanotechnol.*, 2011, **6**, 179–184.
- 48 S. Ross, P. Klement, A. M. Jones, N. J. Ghimire, J. Yan, D. G. Mandrus, T. Taniguchi, K. Watanabe, K. Kitamura, W. Yao, D. H. Cobden and X. Xu, *Nat. Nanotechnol.*, 2014, **9**, 268–272.
- 49 J. Guo, D. Xie, B. Yang and J. Jiang, *Solid-State Electron.*, 2018, **144**, 1.
- 50 M. Y. Li, C. H. Chen, Y. Shi and L. J. Li, *Mater. Today*, 2016, **19**, 322–335.
- 51 Z. Yang, L. Liao, F. Gong, F. Wang, Z. Wang, X. Liu, X. Xiao, W. Hu, J. He and X. Duan, *Nano Energy*, 2018, **49**, 103.
- 52 T. Shen, J. C. Ren, X. Liu, S. Li and W. Liu, *J. Am. Chem. Soc.*, 2019, **141**, 3110.
- 53 A. Li, Q. Chen, P. Wang, Y. Gan, T. Qi, P. Wang, F. Tang, J. Z. Wu, R. Chen, L. Zhang and Y. Gong, *Adv. Mater.*, 2019, **31**, 1805656.
- 54 N. N. Mude, R. N. Bukke and J. Jang, *Adv. Mater. Technol.*, 2022, 2101434.
- 55 Z. Cheng, *et al.*, *J. Mater. Chem. C*, 2022, **10**, 1511–1516.
- 56 N. R. Pradhan, J. Ludwig, Z. Lu, D. Rhodes, M. M. Bishop, K. Thirunavukkuarasu, S. A. McGill, D. Smirnov and L. Balicas, *ACS Appl. Mater. Interfaces*, 2015, **7**(22), 12080–12088.
- 57 H. Li, L. Ye and J. Xu, *ACS Photonics*, 2017, **4**, 823.
- 58 H. Im and S. Kim, *Adv. Electron. Mater.*, 2021, **7**, 2100003.
- 59 P. Lin, L. Zhu, D. Li, L. Xu, C. Pan and Z. Wang, *Adv. Funct. Mater.*, 2018, **28**, 1802849.

